QUASI-GEOSTROPHIC DIAGNOSIS OF THE INFLUENCE OF VORTICITY ADVECTION ON THE DEVELOPMENT OF UPPER LEVEL JET-FRONT SYSTEMS

by

JONATHAN E. MARTIN

Department of Atmospheric and Oceanic Sciences
University of Wisconsin-Madison
1225 W. Dayton Street
Madison, WI 53705
jemarti1@wisc.edu
(608) 262-9845

Submitted for publication in *Quarterly Journal of the Royal Meteorological Society*:
25 July 2013
Revised version submitted 20 November 2013
Second revision submitted 7 January 2014

ABSTRACT

A partition of the geostrophic vorticity into shear and curvature components is employed to consider the influence of differential vorticity advection on the development of upper level jet-front systems in northwesterly flow in an idealized and an observed case. The analysis reveals that negative geostrophic shear vorticity advection by the thermal wind, inextricably coincident with regions of geostrophic cold air advection in cyclonic shear, forces subsidence that is distributed in narrow, quasi-linear, frontal scale bands aligned along the warm edge of the upper baroclinic zone. In each case examined, this component of the quasi-geostrophic (QG) subsidence makes the largest contribution to upper frontogenetical tilting.

Additionally, since QG omega forced by geostrophic vorticity advection by the thermal wind is of the shearwise variety, the analysis shows that the traditional emphasis on the role of laterally displaced transverse circulations is an incomplete description of the upper frontogenetic tilting that arises in such environments. In fact, the results suggest that Mudrick's (1974) emphasis on negative vorticity advection increasing with height combined with Shapiro's (1981) insight regarding the lateral displacement of frontogenetic transverse circulations offers the most comprehensive way to conceptualize the forcings that promote rapid upper level jet-front development in regions of geostrophic cold air advection in cyclonic shear.

1. Introduction

Careful analysis of radiosonde observations of the upper troposphere by Reed and Sanders (1953), Newton (1954), Reed (1955), and Reed and Danielsen (1959) revealed the existence of upper tropospheric frontal structures that were essentially independent of the more conventional surface-based frontal zones first emphasized in the Norwegian Cyclone Model (Bjerknes and Solberg 1922). These upper-level fronts were found to be of synoptic-scale length but mesoscale width and characterized by locally strong horizontal and vertical shear like their surface-based counterparts. It was hypothesized in these contributions that differential vertical motion, with subsidence preferentially on the warm side of an upper level baroclinic zone, was responsible for tilting vertical shear and vertical potential temperature gradients into the horizontal. Additional evidence for the centrality of tilting in the genesis of upper-level fronts was the fact that these features routinely exhibited downward extrusions of stratospheric air (manifest in high values of potential vorticity (PV) as well as radioactivity) into the upper troposphere beneath the tropopause-level jet core (Reed and Danielsen 1959).

The importance of understanding the processes by which these upper level fronts develop derives from their influence on a number of important meteorological phenomena. By virtue of their association with extrusion of stratospheric potential vorticity (PV) into the middle and upper troposphere, upper fronts have been examined as the progenitors of the mid-tropospheric waves (i.e.

vorticity maxima) directly associated with lower tropospheric development (e.g. Uccellini et al. 1985, Sanders 1988, Lackmann et al. 1997). Upper fronts are also primary conduits of stratospheric/tropospheric exchange (e.g. Danielsen 1964, Shapiro 1980, Stohl et al. 2003). Finally, the upper frontogenesis process involves substantial deformation of the tropopause, both above and below the jet core and so contributes to the structure and evolution of lower stratospheric frontal zones (Lang and Martin 2012).

Much of the work regarding upper frontal development since the pioneering studies of the 1950s has considered the synoptic-scale environments within which the requisite differential vertical motions might develop. Three dimensional channel models of growing baroclinic waves repeatedly show that the phase difference between the pressure and thermal waves results in a tendency for geostrophic cold air advection along the downstream portions of upper-level baroclinic zones in northwesterly flow (e.g. Mudrick 1974, Buzzi et al 1977, Newton and Trevisan 1984, Rotunno et al. 1994).

Mudrick (1974) examined the upper frontogenesis process in northwesterly flow using the output from an idealized channel model. Employing both quasi-geostrophic (QG) and primitive equation (PE) simulations, he found that in both cases the strongest descent in the middle and upper troposphere was located beneath the jet core. This subsidence contributed to the tilting of isentropes as well as horizontal vortex tubes in such a way as to intensify the horizontal temperature contrast and sharpen the jet. Mudrick diagnosed the frontogenetic subsidence as

resulting from a combination of vorticity advection decreasing with height[1] and the subsidence branch of a thermally direct vertical circulation associated with confluent frontogenesis. It is clear that, though he references this combination of forcings, the predominant forcing in the Mudrick conceptual model is the vorticity advection. Indeed, he argued that subsidence through the jet core, via tilting, serves to increase the cross-jet vorticity gradient by simultaneously increasing (decreasing) the relative vorticity on the cyclonic (anticyclonic) shear side, thus providing an environment in which the NVA driving the subsidence might be intensified. A similar positive feedback mechanism was diagnosed for a hierarchy of approximations by Keyser and Pecnick (1985b) and Reeder and Keyser (1988).

Shapiro (1981, 1983) considered the effect of both confluence and horizontal shear on upper frontogenesis from the perspective of the Sawyer (1956)-Eliassen (1962) circulation equation. He argued that the effect of horizontal shear on a positive along-front thermal gradient (i.e. geostrophic cold air advection) was to displace the thermally direct circulation associated with the confluent frontogenesis toward the warm side of developing upper-fronts (Rotunno et al. 1994 referred to this as the Shapiro effect). Such lateral displacement placed the subsidence branch of the circulation on the warm side of the upper baroclinic zone, promoted frontogenetical tilting, and gave it the appearance of being thermally indirect.

[1] Specifically, Mudrick (1974) indicts " . . a region of NVA, the magnitude of which increases with height below the jet core . ."

Keyser and Pecnick (1985a) employed a two-dimensional primitive equation model to investigate quantitatively the effect of this combination of confluence and horizontal shear on the development of fronts near the tropopause. They found that in the case of geostrophic cold air advection in cyclonic shear, a well-defined front developed first at the tropopause and then extended into the mid-troposphere. This development was dominated by tilting provided by a circulation that was interpreted as a thermally direct cross-front ageostrophic circulation displaced far enough into the warm air to place the maximum subsidence in the mid-troposphere within and to the warm side of the developing frontal zone. A noteworthy result of this work was that, despite its purely 2D approach, the resulting structures closely resembled those discovered in the aforementioned observational studies. In other words, the effect of flow curvature on the resulting vertical motion field was not required to reproduce realistic frontal structures.

The theoretical/observational studies of Shapiro and the modeling studies of Keyser and collaborators (e.g. Keyser and Pecnick 1985a,b, Keyser and Shapiro 1986, Reeder and Keyser 1988, Pecnick and Keyser 1989, Keyser et al. 1992a, Keyser 1999) focus on upper frontogenetic tilting forced by transverse[2] circulations that arise from horizontal frontogenesis (frontolysis) associated with confluence and horizontal shear. In these studies, which have contributed greatly to modern understanding of the upper frontogenesis process, the lateral shift of these transverse circulations toward the warmer or colder air has been emphasized. An

[2] Here, *transverse* refers to couplets of ascent and descent that straddle the geostrophic flow.

unintended, but nonetheless unfortunate, consequence of this focus has been a lack of emphasis on the role of differential vorticity advection in the upper frontogenesis process as outlined by Mudrick (1974). Vorticity advection by the thermal wind is a component of what Martin (2006) referred to as the shearwise omega (ω_s). Since ω_s is forced by convergence of the along-isentrope component of the $\boldsymbol{Q}$-vector, it is associated with the *rotation* of $\nabla\theta$ (often referred to as "rotational frontogenesis"), not changes in its magnitude (Keyser et al. 1992). Henceforth, "frontogenesis" will refer only to the process of changing $|\nabla\theta|$. In this paper we show that the Shapiro effect – operation of horizontal shear on a positive along-front thermal gradient – is associated with a vertical circulation that responds to both frontogenesis and vorticity advection by the thermal wind which are physically distinct forcings. In fact, it is demonstrated that the predominant sinking motion that drives upper frontogenesis in such synoptic environments can be related to negative geostrophic shear vorticity advection by the thermal wind.

The paper is organized in the following manner. A review of the nature of shearwise and transverse QG vertical motions is given in Section 2. As a component of that review it is demonstrated that vorticity advection by the thermal wind is a distinctly shearwise species of QG vertical motion. Also in Section 2, the partition of the geostrophic vorticity into its shear and curvature components is described and a method for calculating the QG vertical motions associated with each portion of the vorticity is presented. Section 3 contains analyses of two cases - one an idealized numerical simulation, the other an observed case – that demonstrate the influence of shear vorticity advection by the thermal wind on the development of upper level

jet-front systems. Conclusions are presented in Section 4 along with discussion of the results and suggestions for future work.

2. Theoretical background and methodology

a. Vertical motions associated with jet streaks

Keyser et al. (1992b) demonstrated that the total quasi-geostrophic (QG) vertical motion could be partitioned into orthogonal portions associated with the across- and along-isentrope ***Q***-vector divergence, ω_n and ω_s, respectively. They concluded that the characteristic comma-shaped vertical motion distribution of the mid-latitude cyclone arises from the modification of a cellular (ω_s) dipole pattern by the banded (ω_n) dipoles associated with frontal zones. It is important to note that ω_n is precisely the vertical motion associated with geostrophic frontogenesis. To emphasize their orientations to the thermal wind (i.e. the geostrophic vertical shear), Martin (2006) referred to ω_s and ω_n as the shearwise (along shear) and transverse (across shear) QG vertical motions, respectively. He demonstrated that lower-tropospheric cyclogenesis responds predominantly to column stretching associated with the updraft portion of the shearwise QG vertical motion.

This suggestion is consistent with the insight of Sutcliffe (1947) who demonstrated that a significant portion of the synoptic-scale upward vertical motion could be attributed to cyclonic vorticity advection by the thermal wind ($-\vec{V}_T \cdot \nabla \zeta_g$). Since the geostrophic wind is non-divergent on an *f*-plane, this is equivalent to the flux divergence of the vector $\vec{V}_T \zeta_g$ which, by definition, is aligned parallel to the

geostrophic vertical shear. Consequently, any vertical motion associated with vorticity advection by the thermal wind is of the shearwise variety and has no relationship to frontogenesis.

In order to demonstrate that the Shapiro effect involves two physically distinct forcings for QG omega, the ***Q***-vector distribution in a region of geostrophic cold air advection in cyclonic shear is illustrated in Fig. 1. Following Sanders and Hoskins (1990), the ***Q***-vector can be written as

$$\vec{Q} = -f\gamma \left| \frac{\partial \theta}{\partial n} \right| \left[\hat{k} \times \frac{\partial \vec{V}_g}{\partial s} \right] \qquad (1)$$

where $\gamma = \frac{R}{f p_o} \left(\frac{p_o}{p}\right)^{c_v / c_p}$, the $\hat{n}$ axis points into the cold air and $\hat{s}$ is along the isentropes as indicated. The geostrophically forced vertical circulation in such an environment is composed of both a tranverse[3] portion (associated with $\boldsymbol{Q_n}$) and a shearwise portion (associated with $\boldsymbol{Q_s}$). When the isentropes are fairly straight, a substantial fraction of the shearwise circulation in such an environment can be shown to be related to vorticity advection by the thermal wind (Martin 1999).

Additional precision into the nature of vorticity advection by the thermal wind is afforded by partitioning the geostrophic vorticity into components associated with shear and curvature. Such a partitioning proceeds from consideration of the natural coordinate expression for the vorticity (Holton 1979);

---

[3] Here, *transverse* refers to couplets of ascent and descent that straddle the geostrophic vertical shear.

$$\zeta_g = -\frac{\partial V}{\partial n} + \frac{V}{R_s} \qquad (2)$$

where V is the magnitude of the geostrophic wind speed, R_s is the radius of curvature of the streamlines (e.g. geopotential height contours), and $\hat{n}$ is the unit vector direction 90° to the left of the wind direction. Bell and Keyser (1993) provide transformations of the natural coordinate components in (2) into Cartesian coordinates more amenable for calculation from gridded data. Specifically, the shear vorticity is given by

$$-\frac{\partial V}{\partial n} = -\frac{1}{V^2}[u_g{}^2(\frac{\partial u_g}{\partial y}) - v_g{}^2(\frac{\partial v_g}{\partial x}) - (u_g v_g)(\frac{\partial u_g}{\partial x} - \frac{\partial v_g}{\partial y})] \qquad (3a)$$

while the curvature vorticity is given by

$$\frac{V}{R_s} = \frac{1}{V^2}[u_g{}^2(\frac{\partial v_g}{\partial x}) - v_g{}^2(\frac{\partial u_g}{\partial y}) - (u_g v_g)(\frac{\partial u_g}{\partial x} - \frac{\partial v_g}{\partial y})]. \qquad (3b)$$

Following Hoskins and Pedder (1980), Martin (2006) showed that the forcing for QG omega associated with thermal wind advection of vorticity can be written as twice the convergence of a vector, $\vec{Q}_{TR}$[4], given by

$$\vec{Q}_{TR} = f_o \gamma \zeta_g (k \times \nabla\theta). \qquad (4)$$

Using the expressions for the shear ($\zeta_{g_{shear}}$) and curvature ($\zeta_{g_{curv}}$) contributions to the geostrophic vorticity, the forcing for QG vertical motion associated with each

[4] The subscript "*TR*" refers to the work of Trenberth (1978) that emphasizes the role of thermal wind advection of geostrophic vorticity in forcing QG omega.

component can therefore be written as $-2\nabla\cdot\vec{Q}_{TR_{shear}}$ and $-2\nabla\cdot\vec{Q}_{TR_{curv}}$ where $\vec{Q}_{TR_{shear}} = f_o\gamma\zeta_{g_{shear}}(\hat{k}\times\nabla\theta)$ and $\vec{Q}_{TR_{curv}} = f_o\gamma\zeta_{g_{curv}}(\hat{k}\times\nabla\theta)$.

It is instructive to consider these forcing terms in some iconic synoptic environments. Figure 2 depicts aspects of a straight jet streak with no geostrophic temperature advection at the jet core. There are three separate forcings that contribute to the vertical circulation about the entrance and exit regions of this schematic jet streak. First, by virtue of the isolated nature of the geostrophic wind speed maxima, there has to be some streamline curvature in the flow such that confluence characterizes the entrance region and diffluence the exit region. Consequently, the curvature vorticity maxima and minima are located poleward and equatorward of the jet core, respectively (Fig. 2a). Thermal wind advection of the curvature vorticity clearly contributes to the classic four-quadrant jet streak circulation. The shear vorticity is positive (negative) everywhere poleward (equatorward) of the jet axis but it is non-uniform along the jet axis as a consequence of the non-uniform geostrophic wind speed along the jet (Fig. 2b). The maxima and minima of shear vorticity are located poleward and equatorward of the jet core, respectively – perfectly co-located with the curvature maxima and minima. The shear vorticity advection in the entrance (exit) region of the jet produces a thermally direct (indirect) vertical circulation, in concert with that associated with the curvature vorticity advection. Finally, the confluence (diffluence) in the entrance (exit) region, associated with horizontal frontogenesis (frontolysis), forces a thermally direct (indirect) vertical circulation that is in phase with the circulation

forced by vorticity advection (Fig. 2c). Thus, the classic four-quadrant vertical motion distribution is seen to be the result of both shearwise (vorticity advection forcings) and transverse (frontogenetical forcings) vertical motions.

Taking the case of geostrophic cold air advection along the jet axis, as considered by Shapiro (1981, 1982) (see Fig. 3b in Shapiro 1982) and illustrated in Fig. 3, the thermal wind is directed from WSW to ESE, parallel to the schematic isentropes. It follows that locations upshear (downshear) of the geostrophic curvature vorticity maxima will be characterized by subsidence (ascent) while the opposite ω distribution attends the geostrophic curvature vorticity minima (Fig. 3a). The gradient of geostrophic shear vorticity along the thermal wind is particularly strong near the jet core resulting, again, in a band of forcing for subsidence, along the length of the jet core, contributed by shear vorticity advection by the thermal wind (Fig. 3b). Meanwhile, the confluent geostrophic frontogenesis and diffluent geostrophic frontolysis associated with the entrance and exit regions, respectively, are centered on the isentrope that makes the smallest angle with the geostrophic streamlines in those regions. Given the northeast to southwest orientation of the isentropes in the geostrophic cold air advection scenario depicted in Fig. 3, that location is shifted to the southern side of the jet entrance region and to the northern side of the jet exit region (Fig. 3c). As a consequence, the thermally direct entrance (indirect exit) region circulation is shifted southward (northward) such that the subsidence branch is located over the jet core. Once again, these three components of the total vertical motion are distributed in such a way as to encourage a single, subsiding current through the jet core, a circulation that has been shown to be

central to the development of upper level jet-front systems (e.g. Keyser and Pecnick 1985). It is a straightforward extrapolation of the above argument to note that for jet streaks of synoptic-scale length (where the radius of curvature in the geopotential height contours is large), curvature vorticity advection will make a meager contribution to the vertical motions. Importantly, this schematic analysis affirms that the vertical circulation that drives upper frontogenetic tilting is composed of both shearwise and transverse components – a conceptual departure from the singular emphasis on transverse circulations that has dominated the investigation of upper frontogenetic tilting in the previous literature. The goal of this paper is to determine the relative contributions to upper frontogenesis made by each component.

b. Calculation of QG omega

In the subsequent section, gridded analyses from the National Center for Environmental Prediction's (NCEP's) Global Forecast System (GFS) model as well as output from an idealized simulation of the University of Wisconsin Non-Hydrostatic Modeling System (UW-NMS, Tripoli 1992) are used in the calculation of the QG omega. The idealized simulations were carried out using an adiabatic channel model version of the UW-NMS (Tripoli 1992) employing an analytic initialization scheme based upon formulations by Fritsch et al. (1980), Nuss and Anthes (1987) and Cao and Cho (1995). The simulations were run on a spherical grid with resolution 126 x 100 km at the equator over a domain 5800 x 6000 km centered at 38° N. Forty vertical levels were used with *dz* starting at 300 m and stretching to

600 m above the first 12 grid levels. The model top (at 20.5 km) included a Rayleigh friction zone while the bottom was flat and homogeneous with a Businger surface layer. A first order turbulence closure scheme was used. The initialization specifies a zonal jet with a 4000 km moderate amplitude sinusoidal perturbation in temperature and pressure imposed upon it, along with a height invariant lateral shear[5] of 4.5 x 10^{-5} s^{-1} similar to that used in the LC2 experiments of Thorncroft et al. (1993). The integrations were run for 96 h.

In the calculation of omega, the gridded analyses from the GFS and forecast output from the UW-NMS are first bi-linearly interpolated from their original output grids to a 1° x 1° latitude/longitude grid at 19 isobaric levels from 1000 to 100 hPa at 50 hPa increments using an interpolation program included in the General Meteorology Package (GEMPAK). The grid-point height and temperature data were then subjected to a Gaussian smoother that eliminates roughly 2/3 of the energy at wavelengths ≤ 660 km, yielding results similar to those achieved using the cowbell filter described by Barnes et al. (1996) for use in quasi-geostrophic diagnostics with mesoscale models. Employing the technique of successive over relaxation (SOR),

$$\sigma(\nabla^2 + \frac{{f_o}^2}{\sigma}\frac{\partial^2}{\partial p^2})\omega = -2\nabla\cdot\vec{Q} \qquad (5a)$$

$$= -2\nabla\cdot\vec{Q}_n \qquad (5b)$$

$$= -2\nabla\cdot\vec{Q}_s \qquad (5c)$$

$$= -2\nabla\cdot\vec{Q}_{TR_{curv}} \qquad (5d)$$

$$= -2\nabla\cdot\vec{Q}_{TR_{shear}} \qquad (5e)$$

[5] A domain-wide, barotropic shear of 20 m s^{-1} was distributed over 40° of latitude (from 20° N to 60° N).

the *f*-plane version of the QG omega equation is solved using a spatially averaged static stability that varies for each time with f_o set equal to the central latitude of the domain for each of the cases examined. With geostrophic forcing corresponding to the divergences of $\boldsymbol{Q}$, $\boldsymbol{Q_n}$, and $\boldsymbol{Q_s}$, the total (5a), transverse (5b), and shearwise (5c) QG vertical motions, respectively, are returned in units of Pa s^{-1}. Those portions of the shearwise QG omega associated with curvature and shear vorticity advection by the thermal wind are calculated separately using (5d) and (5e), respectively. The author knows of no prior study that has separately calculated these last two species of the QG omega. Next, the separate roles of shear and curvature vorticity advection by the thermal wind as well as horizontal confluence/diffluence in the production of vertical motions that accomplish upper frontogenetical tilting in the real observed case as well as the idealized simulation are considered.

3. Analysis

In this section, two cases of upper frontogenesis in northwesterly flow are explored. The analysis begins with examination of the idealized simulation.

a. Idealized UW-NMS simulation

The 500 hPa analysis from the 36th hour of the idealized simulation, hereafter referred to as H36, is shown in Fig. 4. The geopotential height and temperature structure in Fig. 4a demonstrates the phase lag between the geopotential trough and the thermal trough that Shapiro (1981) argued is characteristic of developing baroclinic waves. The consequence of this phase shift in the model cyclone is the substantial region of geostrophic cold air advection which begins just downstream

of the ridge crest and continues through the entire length of the trough axis to the downstream thermal ridge axis. Isopleths of the geostrophic vorticity at 500 hPa are also included in Fig. 4a. The orientation of isentropes to isopleths of vorticity demonstrates that from the ridge crest to approximately the base of the trough axis, there is negative vorticity advection by the thermal wind. It also appears that the maximum NVA by the thermal wind is located on the warm side of the 500 hPa baroclinic zone. More precise insight into the distribution of the geostrophic vorticity and the associated QG omega is obtained by partitioning the total vorticity into its shear and curvature components.

The QG omega forced by shear vorticity advection (Fig. 4b) shows a quasi-linear band of maximum subsidence with its axis precisely along the warm edge of the upper baroclinic zone. A similar analysis employing the geostrophic curvature vorticity is shown in Fig. 4c. Here the maximum NVA by the thermal wind is located just upstream of the trough axis and does not exhibit a strong bias toward one side of the baroclinic zone or the other. The resulting subsidence region is more kidney bean-shaped in nature with its long axis displaced slightly toward the warm side of the upper baroclinic zone.

A vertical cross-section along A-A' in Fig. 4a reveals the distribution of the various subsidence maxima associated with the upper frontal development at this time. Shear vorticity advection by the thermal wind forces a narrow, fairly intense downdraft, centered just equatorward of the steepest portion of the dynamic tropopause (indicated by the 1.5 PVU isopleth of potential vorticity) and on the

warm side of the upper tropospheric baroclinic zone (Fig. 5a). This subsidence forces notable tilting frontogenesis ($F_{tilt} = -\frac{\partial \theta}{\partial p}\frac{\partial \omega}{\partial n}$ where $\hat{n}$ points into the cold air) in the developing upper frontal zone (Fig. 5b). A substantially different distribution of subsidence, associated with curvature vorticity advection, is shown in Fig. 5c. This more isotropic distribution, centered at a lower elevation, does considerably less tilting frontogenesis than that associated with shear vorticity advection (Fig. 5d). Finally, the QG vertical motion associated with geostrophic horizontal frontogenesis (referred to as ω_n by Keyser et al. (1992b) and transverse ω by Martin (2006)) responds to the presence of a horizontal frontogenesis maxima displaced to the warm side of the upper baroclinic zone and exhibits a similar geometry to the subsidence associated with the shear vorticity advection (Fig. 5e) with smaller magnitude and displacement further toward the cold side of the upper baroclinic zone. Consequently, although the QG frontogenetic transverse circulation does contribute to tilting frontogenesis (Fig. 5f), it does less than 30% as much tilting as the subsidence associated with the shear vorticity advection.

The relative contributions of the various categories of QG subsidence remain the same at a later time in the development of the idealized storm. At H42, both the thermal and vortex structures of the storm are more intense. The 500 hPa geopotential and temperature analysis at H42 (Fig. 6a) illustrates the continued presence of geostrophic cold air advection in the northwesterly flow from roughly the ridge crest to the eastern flank of the closed upper low. Once again, the region of strongest negative vorticity advection by the thermal wind is along the warm edge

of the upper baroclinic zone and most of that is related to the shear vorticity (Fig. 6b). The result of this forcing is an even more elongated linear band of subsidence on the warm edge of the upper front (Fig. 6b). The curvature vorticity contribution looks nearly identical to that from H36 with a nearly identical distribution of associated QG vertical motion (Fig. 6c).

Vertical cross-sections of QG ω and associated tilting frontogenesis along B-B' in Fig. 6a are shown in Fig. 7. As before, the subsidence associated with shear vorticity advection is centered on the warm side of the upper baroclinic zone just equatorward of the PV extrusion, is restricted horizontally, and lies beneath the jet core (Fig. 7a). The associated tilting frontogenesis is very strong throughout the middle and upper troposphere (Fig. 7b). The subsidence associated with the curvature vorticity advection is centered at a lower elevation, is more isotropic in shape, and more or less centered on the upper baroclinic zone (Fig. 7c). Consequently, this subsidence does very little tilting frontogenesis (Fig. 7d). Finally, the QG transverse circulation (Fig. 7e) is nearly centered on the upper baroclinic zone as well and is fairly weak. Its associated tilting frontogenesis is both weak and restricted to the upper troposphere (Fig. 7f).

b. Observed case: 8 April 2013

An intense upper-level jet front system developed in northwesterly flow just off the west coast of North America on 8 April 2013. This event is fairly representative of northwesterly flow cases that affect western and central North America during the cold season (Lang and Martin 2013). At 0000 UTC 8 April, the

baroclinic zone involved in the frontogenesis was clearly evident at 500 hPa and had a geostrophic vorticity maximum along its entire length (Fig. 8a). Modest geostrophic cold air advection was restricted to the southwest quadrant of the cutoff geopotential low near where the flow was strongly curved.

The 500 hPa QG ω associated with the geostrophic shear vorticity advection exhibited a quasi-linear subsidence feature stretching from northern coastal British Columbia southward to off of the Oregon/California border (Fig. 8b) where the subsidence was maximized on the warm side of the upper baroclinic zone (such was not the case along the northern portion of the subsidence region). Note the substantially isotropic distribution of the associated QG ascent to the southeast. The QG ω associated with the curvature vorticity was focused off the Oregon/California coast and was distributed more isotropically with its maxima centered on the middle of the upper baroclinic zone (Fig. 8c).

A series of vertical cross-sections along C-C` in Fig. 8a are shown in Fig. 9. As was the case in the idealized model simulation, the shear vorticity advection forced a narrow subsidence maxima located directly beneath the jet core on the equatorward side of the PV extrusion (Fig. 9a) which promoted robust tilting frontogenesis within the upper baroclinic zone (Fig. 9b). Though the QG ω associated with curvature vorticity was broader as in the idealized simulation, the gradients of ω on the cold side of the upper baroclinic zone were much stronger in this observed case (Fig. 9c). While this difference produced a more robust contribution to tilting frontogenesis (Fig. 9d), the contribution was focused in the lower stratosphere on the cold side of the developing upper front and did not

penetrate as deeply into the upper troposphere as the contribution from shear vorticity. Finally, the transverse QG ω (Fig. 9e) was displaced to the warm side of the upper baroclinic zone and therefore produced modest tilting frontogenesis in nearly the same location, and to the same vertical depth, as the shear vorticity contribution though with only about half the vigor (Fig. 9f).

Development of the upper level jet-front system continued through 1200 UTC 8 April by which time the magnitude of the 500 hPa temperature gradient had further intensified and the associated geostrophic vorticity strip extended from the central British Columbia coast southward to a robust maxima in southern Nevada (Fig. 10a). Geostrophic cold air advection characterized nearly the entire southern half of the upper front. The QG ω associated with shear vorticity advection was distributed as before with a quasi-linear band of subsidence along the upper baroclinic zone, the southern portion of which was oriented such that the subsidence maxima was displaced toward the warm side of the front (Fig. 10b). The corresponding ascent maximum was more isotropic and centered on the southeastern tip of the baroclinic zone where surface cyclogenesis was beginning (not shown). The curvature vorticity ω was also distributed similarly to the prior time with an intense along-front gradient of vertical motion centered on the trough axis (Fig. 10c). A stubby axis of maximum subsidence upstream of that location was displaced toward the warm side of the upper front.

Vertical cross-sections along line D-D` in Fig. 10a are shown in Fig 11. A narrow, frontal scale region of QG subsidence associated with shear vorticity advection was maximized on the warm side of the upper front, just equatorward of

the deep PV extrusion that extended below 700 hPa by this time (Fig. 11a). This subsidence was responsible for vigorous tilting frontogenesis that extended from the tropopause down to nearly 700 hPa (Fig. 11b). The weakening of what appears to be a rather robust lower stratospheric front by this subsidence is consistent with the findings of Lang and Martin (2012) concerning lower stratospheric fronts in northwesterly flow. A wider, wave-scale subsidence region was associated with curvature vorticity advection and, as at earlier times in this case, the gradient of subsidence was large on the cold side of the upper baroclinic zone (Fig. 11c). The corresponding tilting frontogenesis was concentrated at the jet level and was much weaker in the middle troposphere (Fig. 11d). Finally, though the transverse QG ω was weak, it was displaced toward the warm side of the upper baroclinic zone (Fig. 11e) and contributed substantially to tilting frontogenesis along the upper front (Fig. 11f), though only roughly half as much as the contribution associated with shear vorticity advection.

4. Conclusions

a. Summary of results

In both of the cases examined here (as well as in several others perused during the course of this work), the results are essentially the same. The subsidence associated with geostrophic shear vorticity advection by the thermal wind is always distributed in a narrow, quasi-linear frontal-scale column aligned, where

geostrophic cold air advection prevails, beneath the jet core and along the warm edge of the upper baroclinic zone. The subsidence associated with geostrophic curvature vorticity advection is often of wider horizontal extent, and usually located more nearly in the middle, rather than on the warm side, of the upper baroclinic zone. The couplet of transverse QG ω is, as first recognized by Shapiro (1981), displaced to the warm side of the upper baroclinic zone in regions of geostrophic confluence and shear characterized by geostrophic cold air advection (such as in the northwesterly flow upstream of the upper trough axes in the cases presented here).

The simultaneity of regions of negative vorticity advection increasing with height (i.e. NVA by the thermal wind) and upper tropospheric cold air advection in the upper-frontal environment was first noted by Mudrick (1974) in an idealized simulation of upper frontogenesis. He argued that the subsidence beneath the jet core that characterized developing upper fronts was the result of NVA increasing with height in that column forced by the cross-isobar flow toward lower pressure (i.e. toward the cyclonic shear side of the jet) induced by frontogenetic confluence upstream of an upper trough. Subsidence maximized through the jet core serves to increase the cross-jet vorticity gradient by simultaneously increasing (decreasing) the relative vorticity on the cyclonic (anticyclonic) shear side. Thus a positive feedback between the confluent frontogenesis and NVA-induced subsidence was suggested. Mudrick (1974) further asserted that subsidence through the jet core was enhanced as a result of a maximum of geostrophic cold air advection at and above jet level. His argument referenced a version of the traditional QG omega equation (see his eq. 11) and was made before Trenberth (1978) demonstrated the

connection between that expression and the Sutcliffe (1947) approximation to it which emphasizes the role of geostrophic vorticity advection by the thermal wind in forcing QG ω. It is now clear that what Mudrick (1974) considered as separate forcings for subsidence actually arise simultaneously out of a common synoptic characteristic of the upper-frontal environment - that is, regions of geostrophic cold air advection in cyclonic shear are always characterized by negative geostrophic vorticity advection by the thermal wind.[6] The foregoing analysis has demonstrated that this forcing results in banded subsidence through the jet core which promotes frontogenetic tilting and extrusion of stratospheric air into the upper troposphere along the tilted isentropes. Moreover, as demonstrated by the present analysis, this component of the subsidence in the upper frontal environment can exceed that associated with the confluent frontogenetic couplet, the displacement of which (by the presence of lateral shear) toward the warm side of the upper baroclinic zone was not expressly considered by Mudrick (1974) but constitutes the physical aspect of the broader Shapiro effect that has perhaps been overemphasized. The analysis presented here suggests that Mudrick's (1974) emphasis on NVA increasing with height combined with Shapiro's (1981) insight regarding the lateral displacement of frontogenetic transverse circulations is the most comprehensive way to conceptualize the forcings that promote rapid upper level jet-front development in regions of geostrophic cold air advection in cyclonic shear.

---

[6] It should be noted that regions of geostrophic cold air advection in cyclonic (anticyclonic) shear or warm air advection in anticyclonic (cyclonic) shear are always characterized by negative (positive) geostrophic vorticity advection by the thermal wind.

b. Discussion

Importantly, the subsidence associated with vorticity advection by the thermal wind is of the shearwise, not transverse, variety. This distinction may have important implications regarding the energetics of upper frontogenesis. Changes in eddy kinetic energy (EKE) are largely controlled by divergence of ageostrophic geopotential flux and baroclinic conversion (Orlanski and Sheldon 1995). Of these two processes, only baroclinic conversion can generate new EKE through the action of vertical circulations as described by

$$\frac{\partial(EKE)}{\partial t} = -\omega\alpha$$

where ω and α are the perturbation vertical motion and specific volume, respectively. Thus, thermally direct (indirect) vertical circulations convert available potential energy (APE) to EKE (create APE from EKE). Since any species of shearwise QG ω is forced by convergence of an along-isentrope component of the ***Q***-vector, the resulting ω is distributed in couplets oriented along the geostrophic vertical shear. Such a distribution may render shearwise ω less efficient at baroclinic conversion than transverse ω where the updraft/downdraft couplets may be more predisposed to coincidence with perturbation warm or cold air. It is, therefore, possible that the major contributor to tilting frontogenesis (negative geostrophic shear vorticity advection by the thermal wind) may not play the predominant role in the EKE generation required in the development of upper level jet-front systems. More complete investigation of this issue is left for future work.

The analysis presented in this paper details the forcings for QG ω that operate in the presence of along-flow geostrophic cold air advection. The present paper does not, however, address the *establishment* of the along-flow geostrophic cold air advection itself. That question has been considered in a number of previous contributions (e.g. Rotunno et al. 1994, Schultz and Doswell 1999, Schultz and Sanders 2002, Lang and Martin 2013) and is still at issue. To date, the net result of this debate appears to be verification of the Rotunno et al. (1994) notion that along-flow gradients in subsidence upstream of trough axes are of primary importance in establishing along-flow geostrophic cold air advection. Insight into the origin of the necessary along-flow subsidence gradients may be afforded through adoption of the vorticity partition employed in this paper. Since the evolution to along-flow geostrophic cold air advection from a state of equivalent barotropy depends entirely upon such subsidence gradients, it is worth considering this special case. Certainly, in such a case, variations of curvature vorticity in a wave train are capable of producing a QG ω pattern in which descent is largest immediately upstream (downstream) of an upper trough (ridge) axis. Consequently, a local minimum in QG ω would likely occur near the inflection point between the upstream ridge and downstream trough. The maximum in curvature-induced ω near the trough (ridge) axis would tend to reorient the isentropes in such a way as to promote geostrophic cold (warm) air advection from the trough axis (ridge crest) to somewhere near the inflection point in the upstream (downstream) northwesterly flow. Such a geostrophic temperature advection pattern is often observed in northwesterly flow

(Schultz and Doswell 1999), as illustrated in the case presented by Lang and Martin (2010) (see their Figs. 3 and 4).

On the other hand, shear vorticity advection by the thermal wind in an equivalent barotropic atmosphere would produce a classic four-quadrant pattern in which couplets of vertical motion would straddle the thermal wind at both the entrance and exit regions of jet streaks. Such a distribution of ω would contribute to anticyclonic (cyclonic) rotation of isentropes on the cyclonic (anticyclonic) shear side of the jet (see Eqs. 10b and 11b of Schultz and Doswell 1999). Counteracting these rotations would be the rotation of $\nabla\theta$ on either side of the jet axis provided by the vorticity itself making establishment of along-flow geostrophic temperature advection difficult to achieve. Thus, it is possible that curvature vorticity advection by the thermal wind, by abetting the establishment of geostrophic cold air advection along the flow, activates the shear vorticity advection by the thermal wind that actually drives the subsidence that folds the tropopause, subducts stratospheric air into the troposphere and intensifies the upper level jet-front system. Systematic consideration of this issue requires diagnosis using output from an appropriate idealized model simulation and is currently underway.

Future work will explore the usefulness of the shear/curvature partition employed here in the examination of additional cyclone life cycle diagnoses. These efforts will include consideration of the separate circulations associated with shear and curvature PV derived using the piecewise PV inversion scheme of Davis and Emanuel (1991).

ACKNOWLEDGEMENTS: This research was supported by the National Science Foundation under grant NSF-0950349. The thoughtful comments of two anonymous reviewers are greatly appreciated. Dr. Justin McLay provided the idealized UW-NMS simulations. This paper is dedicated to the memory of Bro. Robert J. Sullivan, C.F.X., a lifelong friend and mentor to the author.

REFERENCES

Barnes, S. L., F. Caracena, and A. Marroquin, 1996: Extracting synoptic-scale diagnostic information from mesoscale models: The Eta model, gravity waves, and quasigeostrophic diagnostics. *Bull. Amer. Meteor. Soc.*, **77**, 519-528.

Bell, G. D., and D. Keyser, 1993: Shear and curvature vorticity and potential-vorticity interchanges: Interpretation and application to a cutoff cyclone event. *Mon. Wea. Rev.*, **121**, 76-102.

Bjerknes, J., and H. Solberg, 1922: Life cycles of cyclones and the polar front theory of atmospheric circulation. *Geofys. Publ*., **3**(1), 1-18.

Bosart, L. F., 1981 The President's Day snowstorm of February 1979: A sub-synoptic scale event. *Mon. Wea. Rev*., **109**, 1542-1566.

Buzzi, A., T. Nanni and M. Taglicazucca, 1977: Mid-tropospheric frontal zones: Numerical experiments with an isentropic coordinate primitive equation model. *Arch. Meteor. Geophys. Bioklim*., **A26**, 155-178.

Cao, Z., and H.-R. Cho, 1995: Generation of moist potential vorticity in extratropical cyclones. *J. Atmos. Sci*., **52**, 3263-3282.

Danielsen, E. F., 1964: *Project Springfield Report*. DASA 1517, Defense Atomic Support Agency: Washington, DC; 97 pp. (DDC).

Davis, C. A., and K. A. Emanuel, 1991: Potential vorticity diagostics of cyclogenesis. *Mon. Wea. Rev*., **119**, 1929-1953.

Eliassen, A., 1962: On the vertical circulation in frontal zones. *Geofys. Publ*., **24**(4), 147-160.

Fritsch, J. M., E. L. Magaziner, and C. F. Chappell, 1980: Analytical initialization for three-dimensional models. *J. Appl. Meteor*., **19**, 809-818.

Gyakum, J. R., 1983a: On the evolution of the *QE II* storm. I: Synoptic aspects. *Mon. Wea. Rev*., **111**, 1137-1155.

_____, 1983b: On the evolution of the *QE II* storm. II: Dynamic and thermodynamic s tructure. *Mon. Wea. Rev*., **111**, 1156-1173.

Holton, J. R., 1979: An Introduction to Dynamic Meteorology. 2nd ed. *International Geophysics Series*, *Vol .23, Academic Press*, 391 pp.

Hoskins, B. J., I. Draghici, and H. C. Davies, 1978: A new look at the **ω**-equation. *Quart. J. Roy. Meteor. Soc*., **104**, 31-38.

_____, and M. A. Pedder, 1980: The diagnosis of mid-latitude synoptic development. *Quart. J. Roy. Meteor. Soc*., **106**, 707-719.

Keyser, D., 1999: On the representation and diagnosis of frontal circulations in two and three dimensions. *The Life Cycles of Extratropical Cyclones*, M. A. Shapiro and S. Gronas, Eds., *Amer. Meteor. Soc*., 239-264.

_____, and M. J. Pecnick, 1985: A two-dimensional primitive equation model of

frontogenesis forced by confluence and horizontal shear. *J. Atmos. Sci*., **42**, 1259-1282.

_____ and M. A. Shapiro, 1986: A review of the structure and dynamics of upper-level frontal zones. *Mon. Wea. Rev*., **114**, 452-499.

_____, B. D. Schmidt and D. G. Duffy, 1992a: Quasigeostrophic diagnosis of three-dimensional ageostrophic circulations in an idealized baroclinic disturbance. *Mon. Wea. Rev*., **120**, 698-730,

_____, _____ and _____, 1992b: Quasigeostrophic vertical motions diagnosed from along- and cross-isentrope components of the Q vector. *Mon. Wea. Rev*., **120**, 731–741.

Lackmann, G. M., D. Keyser, and L. F. Bosart, 1997: A characteristic life cycle of upper-tropospheric cyclogenetic precursors during the Experiment on Rapidly Intensifying Cyclones over the Atlantic (ERICA). *Mon. Wea. Rev*., **125**, 2729-2758.

Lang, A. A., and J. E. Martin, 2010: The influence of rotational frontogenesis and its associated shearwise vertical motions on the development of an upper-level front. *Quart. J. Roy. Meteor. Soc*., **136**, 239-252.

_____, and _____, 2012: The structure and evolution of lower stratospheric frontal zones. Part I: Examples in northwesterly and southwesterly flow. *Quart. J. Roy. Meteor. Soc*. **138**, 1350–1365.

_____, and _____, 2013a: Reply to comments on "The influence of rotational frontogenesis and its associated shearwise vertical motions on the development of an upper front". *Quart. J. Roy. Meteor. Soc*., **139**, 273-279.

_____, and _____, 2013b: The structure and evolution of lower stratospheric frontal zones. Part II: The Influence of tropospheric ascent on lower stratospheric frontal development. *Quart. J. Roy. Meteor. Soc*. **139** (in press).

Martin, J. E., 1999: The separate roles of geostrophic vorticity and deformation in the mid-latitude occlusion process. *Mon. Wea. Rev*., **127**, 2404-2418.

_____, 2006: The role of shearwise and transverse quasigeostrophic vertical motions in the midlatitude cyclone life cycle. *Mon. Wea. Rev*. **134**, 1174–1193.

Mudrick, S. E., 1974: A numerical study of frontogenesis. *J. Atmos. Sci*., **39**, 869-892.

Newton, C. W., 1954: Frontogenesis and frontolysis as a three-dimensional process. *J. Meteor.*, **11**, 449-461.

_____, and A. Trevisan, 1984: Clinogenesis and Frontogenesis in Jet-Stream Waves. Part I: Analytical Relations to Wave Structure. *J. Atmos. Sci*. **41**, 2717- 2734.

Nuss, W. A., and R. A. Anthes, 1987: A numerical investigation of low-level processes in rapid cyclogenesis. *Mon. Wea. Rev*., **115**, 2728-2743.

Orlanski, I., and J. P. Sheldon, 1995: Stages in the energetics of baroclinic systems. *Tellus*, **47A**, 605-628.

Pecnick, M. J., and D. Keyser, 1989: The effect of spatial resolution on the simulation of upper-tropospheric frontogenesis using a sigma-coordinate primitive-equation model. *Meteor. Atmos. Phys*., **40**, 137–149.

Reed. R. J., 1955: A study of a characteristic type of upper-level frontogenesis. *J. Meteor*., **12**, 226-237.

_____ and F. Sanders, 1953: An investigation of the development of a mid-tropospheric frontal zone and its associated vorticity field. *J. Meteor*., **10**, 338-349.

____, and E. F. Danielsen, 1959: Fronts in the vicinity of the tropopause. *Arch. Meteor. Geophys. Bioklim*., **A11**, 1-17.

Reeder, M. J. and D. Keyser, 1988: Balanced and unbalanced upper-level frontogenesis. *J. Atmos. Sci*., **45**, 3366–3386.

Rotunno, R., W. C. Skamarock, and C. Snyder, 1994: An analysis of frontogenesis in numerical simulations of baroclinic waves. *J. Atmos. Sci*., **51**, 3373-3398.

Sanders, F. 1988: Life history of mobile troughs in the upper westerlies. *Mon. Wea. Rev*., **116**: 2629-2648.

Sawyer, J. S., 1956: The vertical circulation at meteorological fronts and its relation to frontogenesis. *Proc. Roy. Soc. London*, **A234**, 346-362.

Schultz, D. M. and C. A. Doswell, 1999: Conceptual models of upper-level frontogenesis in south-westerly and north-westerly flow. *Quart. J. Roy. Meteor. Soc*, **125**, 2535-2562.

_____, and F. Sanders, 2002: Upper-level frontogenesis associated with the birth of mobile troughs in northwesterly flow. *Mon. Wea. Rev*., **130**, 2593-2610.

Shapiro, M. A., 1980: Turbulent mixing within tropopause folds as a mechanism of the exchange of constituents between the stratosphere and troposphere. *J. Atmos. Sci*., **37**, 994-1004.

_____, 1981: Frontogenesis and geostrophically forced secondary circulations in the

vicinity of jet stream-frontal zone systems. *J. Atmos. Sci*., **38**, 954-973.

_____, 1982. Mesoscale Weather Systems of the Central United States. *CIRES Univ. of Colorado/NOAA*, Boulder, Colo, USA. 78 pp.

____, 1983: Mesoscale weather systems of the central United States. *The National STORM Program: Scientific and Technological Bases and Major Objectives*, R. A. Anthes, Ed., 3.1-3.77. [Available from University Corporation for Atmospheric Research, P. O. Box 3000, Boulder, CO 80307.]

Stohl, A., P. Bonasoni, P. Cristofanelli, W. Collins, J. Feichter, A. Frank, C. Forster, E. Gerasopoulos, H. Gäggeler, P. James, T. Kentarchos, S. Kreipl, H. Kolb-Kromp, B. Krüger, C. Land, J. Meloen, A. Papayannis, A. Priller, P. Seibert, M. Sprenger, G.J. Roelofs, E. Scheel, C. Schnabel, P. Seigmund, L. Tobler, T. Trikl, H. Wernli, V. Wirth, P. Zanis, and C. Zerefos, 2003: Stratosphere-troposphere exchange – a review, and what we have learned from STACCATO. *J. Geophys. Res*., **108**, 8516.

Sutcliffe, R. C., 1947: A contribution to the problem of development. *Quart. J. Roy. Meteor. Soc*., **73**, 370-383.

Thorncroft, C. D., B. J. Hoskins, and M. E. McIntyre, 1993: Two paradigms of baroclinic-wave life-cycle behavior. *Quart. J. Roy. Meteor. Soc*., **119**, 17–55.

Trenberth, K. E., 1978: On the interpretation of the diagnostic quasi-geostrophic omega equation. *Mon. Wea. Rev*., **106**, 131-137

Tripoli, G. J., 1992: A nonhydrostatic model designed to simulate scale interaction. *Mon. Wea. Rev*., **120**, 1342-1359.

Uccelllini, L. W., 1986: The possible influence of upstream upper-level baroclinic processes on the development of the QE II storm. *Mon. Wea. Rev*., **114**, 1019-1027.

_____, D. Keyser, K. F. Brill, and D. H. Wash, 1985: The Presidents' Day cyclone of 18-19 February 1979: Influence of upstream trough amplification and associated tropopause folding on rapid cyclogenesis. *Mon. Wea. Rev*., **113**, 962-988.

Whittaker, J. S., L. W. Uccellini, and K. F. Brill, 1988: A model-based diagnostic study of the rapid development phase of the Presidents' Day cyclone. *Mon. Wea. Rev*., **116**, 2337-2365.

FIGURE CAPTIONS

Fig. 1 Schematic of a region of upper tropospheric geostrophic cold air advection in cyclonic shear. Thin gray lines are the geopotential height lines, gray vectors are geostrophic winds, and dashed lines are isentropes with cold air on the left. The ***Q***-vector is indicated in the open shafted arrow with its transverse and shearwise components, ***Qn*** and ***Qs***, indicated in the bold black arrows. See text for additional explanation.

Fig. 2 Schematic straight jet streak with no along-flow geostrophic temperature advection illustrating the vertical circulations associated with (a) geostrophic curvature advection by the thermal wind, (b) geostrophic shear vorticity advection by the thermal wind, and (c) horizontal frontogenesis. Shading represents isotachs with "**J**" indicating the jet core. Dashed lines are isentropes with colder air to the north. Medium solid (dashed) lines are regions of quasi-geostrophic (QG) ascent (descent). In (a) and (c) the bold solid lines are geopotential height lines while in (b) the thin dashed (solid) lines represent schematic contours of positive (negative) geostrophic shear vorticity.

Fig. 3 As for Fig. 2 except for a straight jet characterized by geostrophic cold air advection along its length.

Fig. 4 (a) 36h forecast of 500 hPa geopotential height (bold solid lines), potential temperature (dashed lines) and geostrophic vorticity (shaded and labeled) from the idealized UW-NMS simulation. Vorticity labeled and contoured in units of 2×10^{-5} s^{-1}, beginning at 2×10^{-5} s^{-1}. Geopotential height labeled in m and contoured every 60

m. Potential temperature labeled in K and contoured every 2 K. Vertical cross sections along line A-A` shown in Fig. 5. (b) 36h forecast of 500 hPa geostrophic shear vorticity, potential temperature, and QG ω associated with geostrophic shear vorticity advection by the thermal wind from the UW-NMS idealized simulation. Vorticity shaded and contoured as in Fig. 4a. Potential temperature labeled and contoured as in Fig. 4a. Solid (dashed) lines are 500 hPa QG ω contoured every 1 (-1) dPa s^{-1} starting at 1 (-1) dPa s^{-1}. (c) As for Fig. 4b but for geostrophic curvature vorticity and QG ω associated with geostrophic curvature vorticity advection by the thermal wind. Continents are included only for scale.

Fig. 5 (a) Vertical cross-section along A-A` in Fig. 4a of potential temperature (dashed thin lines), QG subsidence associated with geostrophic shear vorticity advection by the thermal wind (shaded) and the dynamic tropopause (bold line) from the 36h forecast of the UW-NMS idealized simulation. Potential temperature is labeled in K and contoured every 3 K. "**J**" indicates the position of the jet core. QG subsidence contoured every 1 dPa s^{-1} starting at 1 dPa s^{-1}. (b) Vertical cross-section along A-A` in Fig. 4a of potential temperature (labeled and contoured as in Fig. 5a) and tilting frontogenesis associated with the QG subsidence in Fig. 4a from the 36h forecast of the UW-NMS idealized simulation. Thick solid (dashed) lines are positive (negative) tilting frontogenesis contoured every 2 (-2) x 10^{-10} K m^{-1} s^{-1} starting at 2 (-2) x 10^{-10} K m^{-1} s^{-1}. (c) As for Fig. 4a but with shading representing QG subsidence associated with curvature vorticity advection by the thermal wind. (d) As for Fig. 4b but with tilting frontogenesis associated with the subsidence in Fig. 4c. (e) As for Fig. 4a but shading representing QG subsidence associated with geostrophic

horizontal frontogenesis (bold solid lines). Geostrophic frontogenesis contoured every 5 x 10^{-9} K m^{-1} s^{-1} starting at 5 x 10^{-9} K m^{-1} s^{-1}. (f) As for Fig. 4b but with tilting frontogenesis associated with the subsidence in Fig. 4e.

Fig. 6 (a) As for Fig. 4a but from a 42h forecast of the UW-NMS idealized simulation. Vertical cross sections along line B-B` shown in Fig. 7. (b) As for Fig. 4b but from a 42h forecast of the UW-NMS idealized simulation. (c) As for Fig. 4c but from a 42h forecast of the UW-NMS idealized simulation.

Fig. 7 (a) As for Fig. 5a but along B-B` in Fig. 6a with data from the 42h forecast of the UW-NMS idealized simulation. (b) As for Fig. 5b but along B-B` in Fig. 6a with data from the 42h forecast of the UW-NMS idealized simulation. (c) As for Fig. 5c but along B-B` in Fig. 6a with data from the 42h forecast of the UW-NMS idealized simulation. (d) As for Fig. 5d but along B-B` in Fig. 6a with data from the 42h forecast of the UW-NMS idealized simulation. (e) As for Fig. 5e but along B-B` in Fig. 6a with data from the 42h forecast of the UW-NMS idealized simulation. (f) As for Fig. 5f but along B-B` in Fig. 6a with data from the 42h forecast of the UW-NMS idealized simulation.

Fig. 8 (a) 500 hPa geopotential height (bold solid lines), potential temperature (dashed lines) and geostrophic vorticity (shaded) from NCEP's Global Forecast System (GFS) analysis valid at 0000 UTC 8 April 2013. Vorticity labeled and contoured in units of 4 x 10^{-5} s^{-1}, beginning at 4 x 10^{-5} s^{-1}. Geopotential height labeled in m and contoured every 60 m. Potential temperature labeled in K and contoured every 2K. Vertical cross sections along line C-C` shown in Fig. 9. (b) 500

hPa geostrophic shear vorticity, potential temperature, and QG ω associated with geostrophic shear vorticity advection by the thermal wind from the GFS analysis valid at 0000 UTC 8 April 2013. Vorticity shaded and contoured as in Fig. 8a. Potential temperature labeled as in Fig. 8a. but contoured every 4K. Solid (dashed) lines are 500 hPa QG ω contoured every 1 (-1) dPa s^{-1} starting at 1 (-1) dPa s^{-1}. (c) As for Fig. 8b but for geostrophic curvature vorticity and QG ω associated with geostrophic curvature vorticity advection by the thermal wind.

Fig. 9 (a) As for Fig. 5a but along C-C` in Fig. 8a with data from GFS analysis valid at 0000 UTC 8 April 2013. (b) As for Fig. 5b but along C-C` in Fig. 8a with data from the GFS analysis valid at 0000 UTC 8 April 2013. (c) As for Fig. 5c but along C-C` in Fig. 8a with data from the GFS analysis valid at 0000 UTC 8 April 2013. (d) As for Fig. 5d but along C-C` in Fig. 8a with data from the GFS analysis valid at 0000 UTC 8 April 2013. (e) As for Fig. 5e but along C-C` in Fig. 8a with data from the GFS analysis valid at 0000 UTC 8 April 2013. (f) As for Fig. 5f but along C-C` in Fig. 8a with data from the GFS analysis valid at 0000 UTC 8 April 2013.

Fig. 10 (a) As for Fig. 8a but from the GFS analysis valid at 1200 UTC 8 April 2013. Vertical cross sections along line D-D` shown in Fig. 11. (b) As for Fig. 8b but from the GFS analysis valid at 1200 UTC 8 April 2013. (c) As for Fig. 8c but from the GFS analysis valid at 1200 UTC 8 April 2013.

Fig. 11 (a) As for Fig. 5a but along D-D` in Fig. 10a with data from GFS analysis valid at 1200 UTC 8 April 2013. (b) As for Fig. 5b but along D-D` in Fig. 10a with data from the GFS analysis valid at 1200 UTC 8 April 2013. (c) As for Fig. 5c but along D-

D` in Fig. 10a with data from the GFS analysis valid at 1200 UTC 8 April 2013. (d) As for Fig. 5d but along D-D` in Fig. 10a with data from the GFS analysis valid at 1200 UTC 8 April 2013. (e) As for Fig. 5e but along D-D` in Fig. 10a with data from the GFS analysis valid at 1200 UTC 8 April 2013. (f) As for Fig. 5f but along D-D` in Fig. 10a with data from the GFS analysis valid at 1200 UTC 8 April 2013.

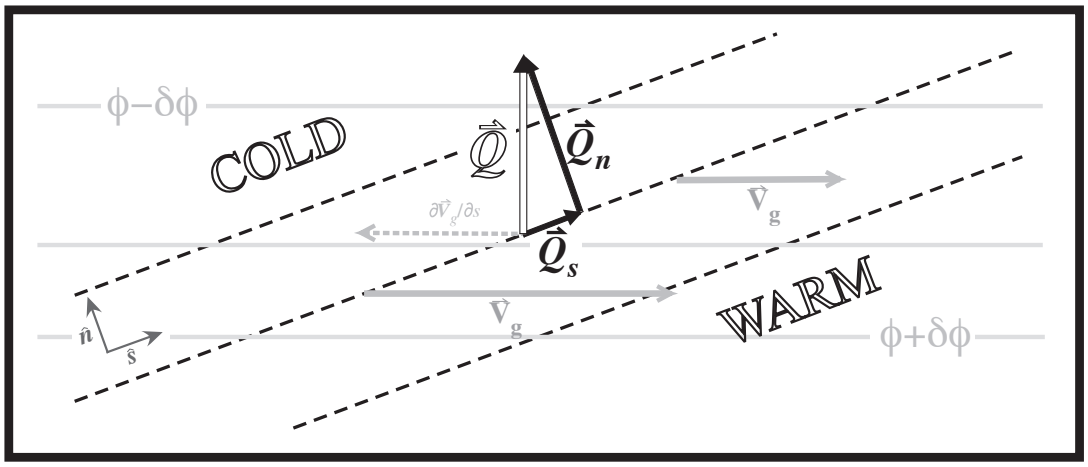

Fig. 1 Schematic of a region of upper tropospheric geostrophic cold air advection in cyclonic shear. Gray solid lines are the geopotential height lines, gray vectors are geostrophic winds, and dashed lines are isentropes with cold air on the left. The $\boldsymbol{Q}$-vector is indicated in the open shafted black arrow with its transverse and shearwise components, $\boldsymbol{Q}_n$ and $\boldsymbol{Q}_s$, indicated in the bold black arrows. See text for additional explanation.

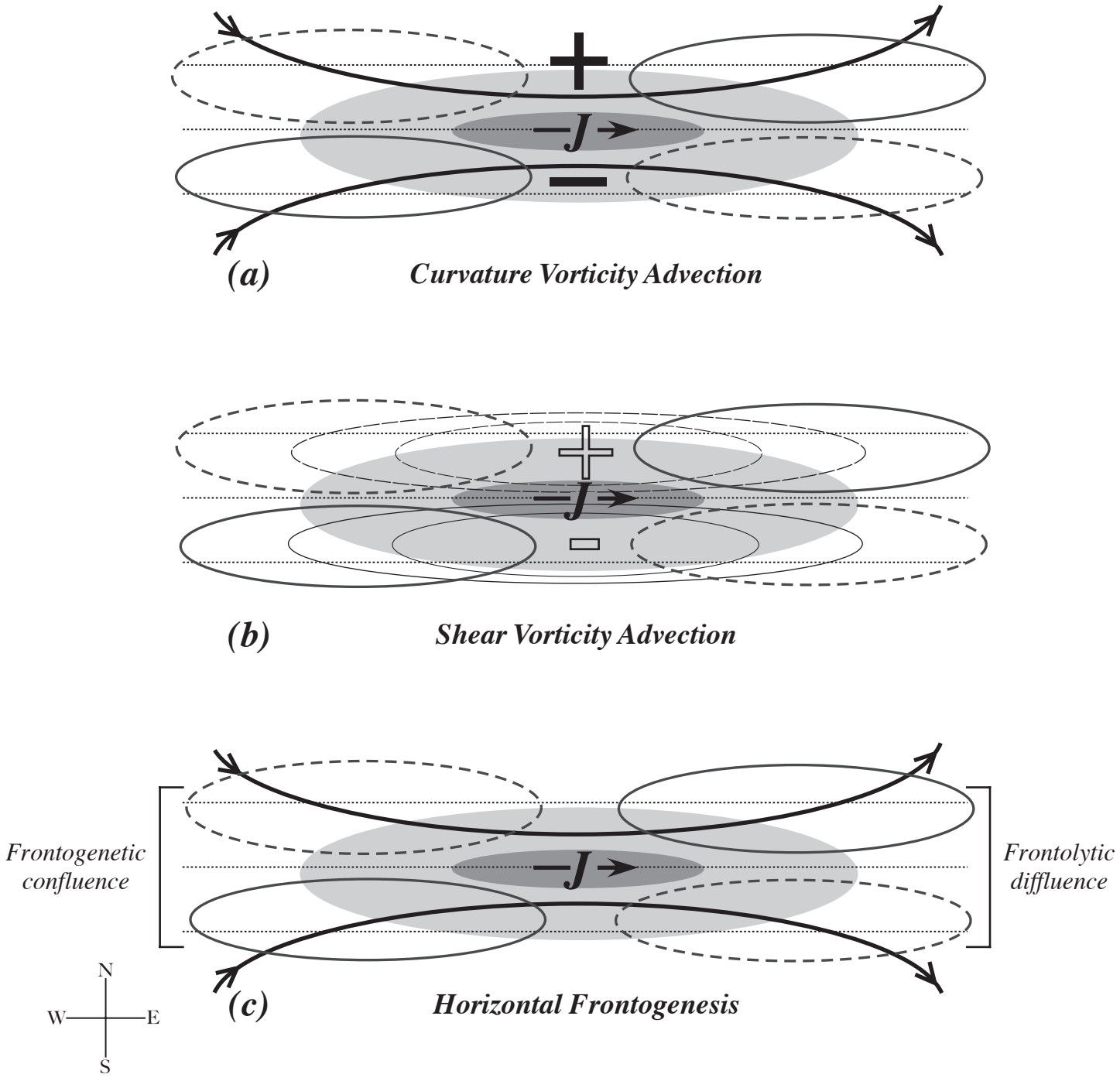

Fig. 2 Schematic straight jet streak with no along-flow geostrophic temperature advection at the jet axis illustrating the vertical circulations associated with (a) geostrophic curvature advection by the thermal wind, (b) geostrophic shear vorticity advection by the thermal wind, and (c) horizontal frontogenesis. Shading represents isotachs with "J" indicating the jet core. Dotted lines are isentropes with colder air to the north. Medium solid (dashed) lines are regions of quasi-geostrophic (QG) ascent (descent). In (a) and (c) the bold solid lines are geopotential height lines while in (b) the thin dashed (solid) lines represent schematic contours of positive (negative) geostrophic shear vorticity.

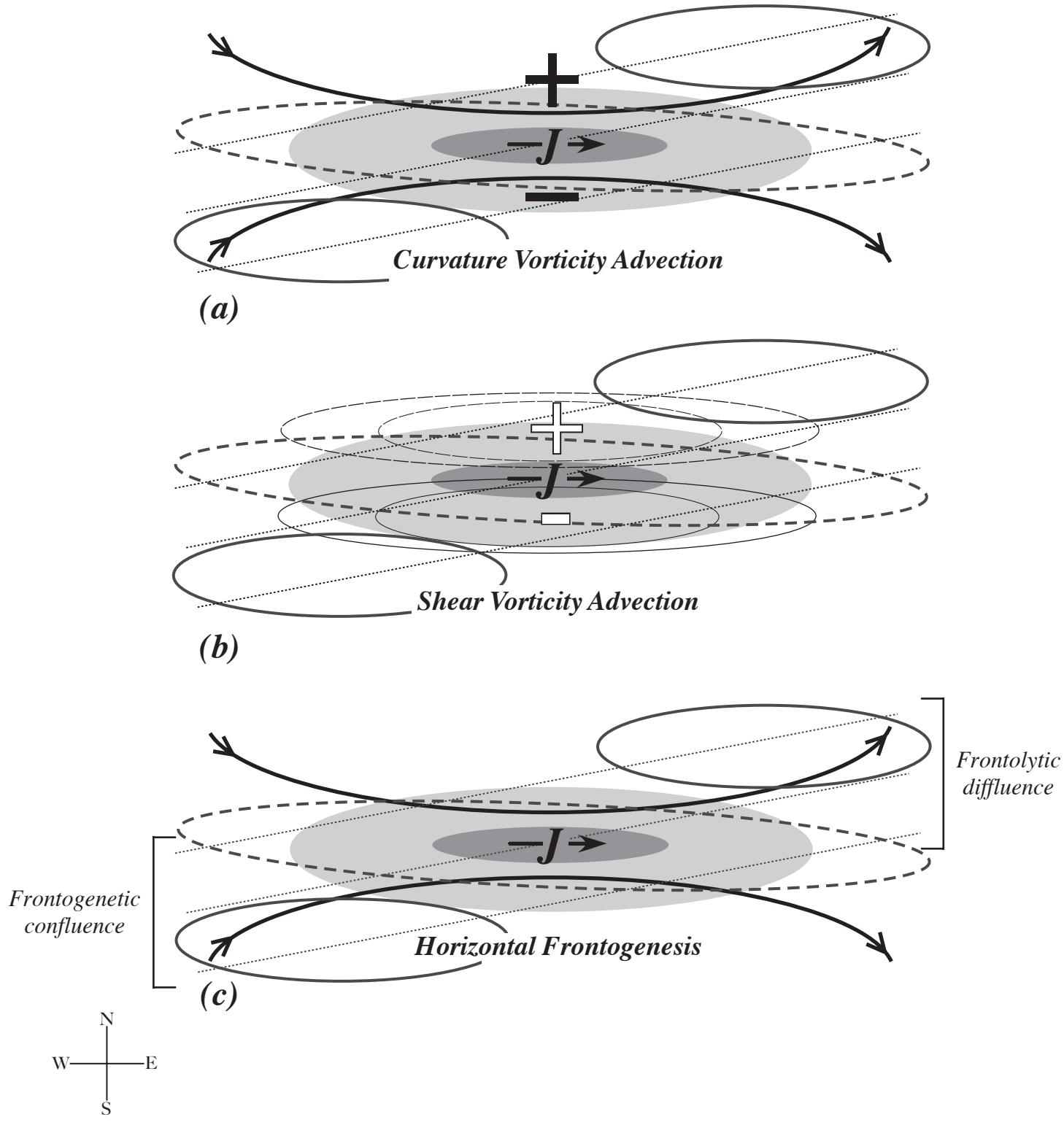

Fig. 3 As for Fig. 2 except for a straight jet characterized by geostrophic cold air advection along its length.

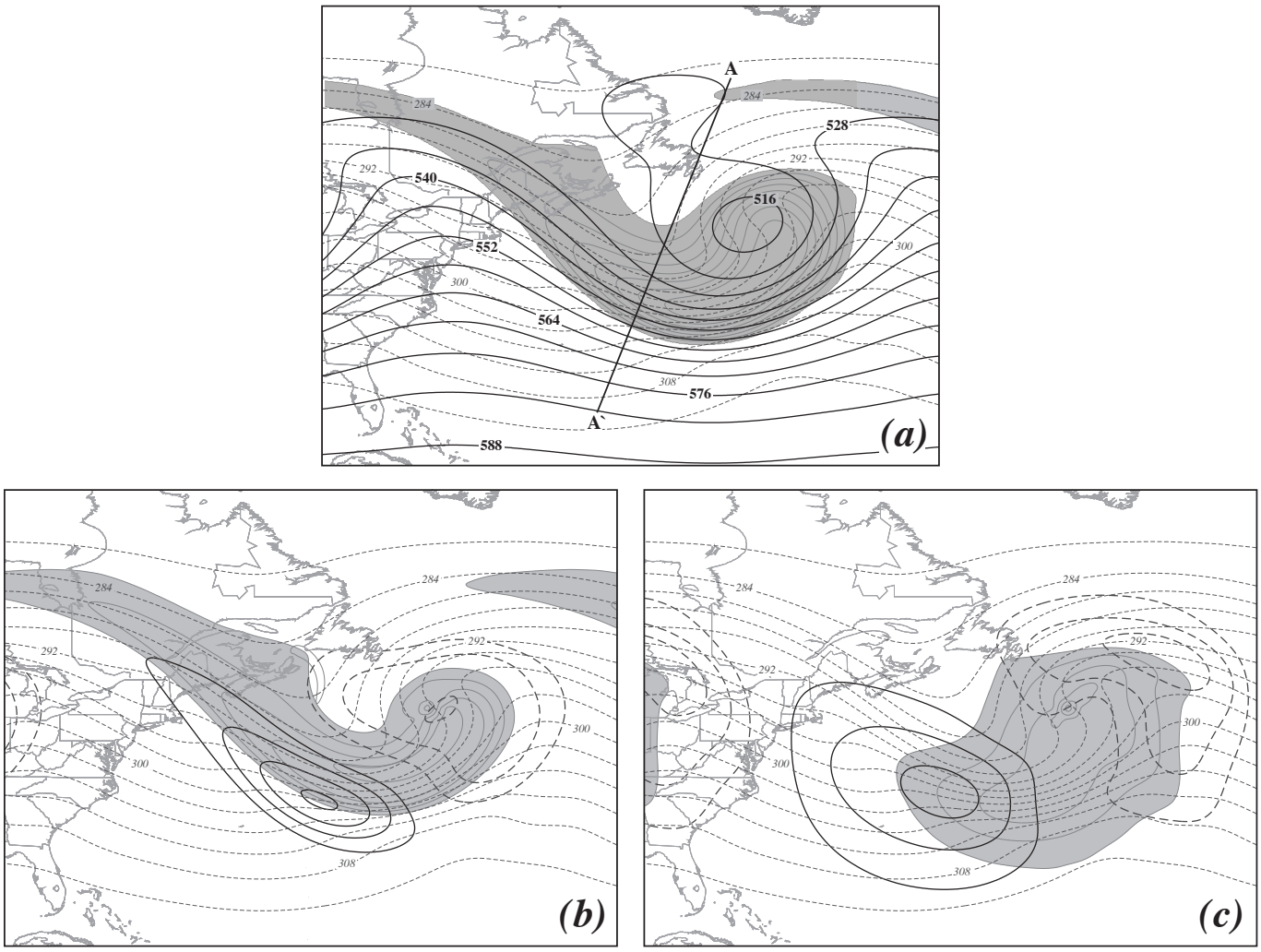

Fig. 4 (a) 36h forecast of 500 hPa geopotential height (bold solid lines), potential temperature (dashed lines) and geostrophic vorticity (shaded and labeled) from the idealized UW-NMS simulation. Vorticity labeled and contoured in units of 2 x 10^{-5} s^{-1}, beginning at 2 x 10^{-5} s^{-1}. Geopotential height labeled in m and contoured every 60 m. Potential temperature labeled in K and contoured every 2 K. Vertical cross sections along line A-A` shown in Fig. 5. (b) 36h forecast of 500 hPa geostrophic shear vorticity, potential temperature, and QG ω associated with geostrophic shear vorticity advection by the thermal wind from the UW-NMS idealized simulation. Vorticity shaded and contoured as in Fig. 4a. Potential temperature labeled and contoured as in Fig. 4a. Solid (dashed) lines are 500 hPa QG ω contoured every 1 (-1) dPa s^{-1} starting at 1 (-1) dPa s^{-1}. (c) As for Fig. 4b but for geostrophic curvature vorticity and QG ω associated with geostrophic curvature vorticity advection by the thermal wind. Continents are included only for scale.

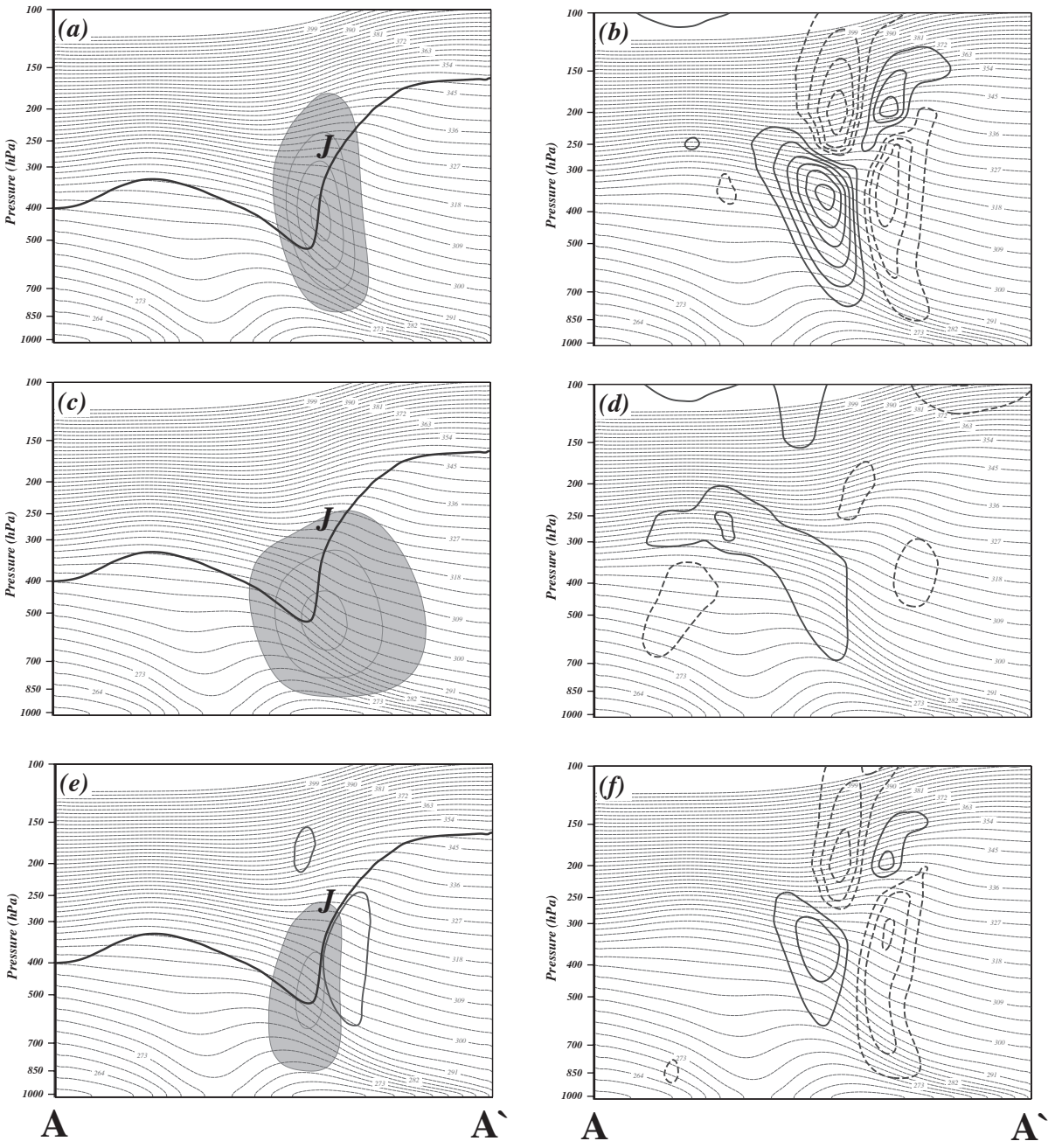

Fig. 5 (a) Vertical cross-section along A-A` in Fig. 4a of potential temperature (dashed thin lines), QG subsidence associated with geostrophic shear vorticity advection by the thermal wind (shaded) and the dynamic tropopause (bold line) from the 36h forecast of the UW-NMS idealized simulation. Potential temperature is labeled in K and contoured every 3 K. "**J**" indicates the position of the jet core. QG subsidence contoured every 1 dPa s^{-1} starting at 1 dPa s^{-1}. (b) Vertical cross-section along A-A` in Fig. 4a of potential temperature (labeled and contoured as in Fig. 5a) and tilting frontogenesis associated with the QG subsidence in Fig. 5a from the 36h forecast of the UW-NMS idealized simulation. Thick solid (dashed) lines are positive (negative) tilting frontogenesis contoured every 2 (-2) x 10^{-10} K m^{-1} s^{-1} starting at 2 (-2) x 10^{-10} K m^{-1} s^{-1}. (c) As for Fig. 5a but with shading representing QG subsidence associated with curvature vorticity advection by the thermal wind. (d) As for Fig. 5b but with tilting frontogenesis associated with the subsidence in Fig. 5c. (e) As for Fig. 5a but shading representing QG subsidence associated with geostrophic horizontal frontogenesis (bold solid lines). Geostrophic frontogenesis contoured every 5 x 10^{-9} K m^{-1} s^{-1} starting at 5 x 10^{-9} K m^{-1} s^{-1}. (f) As for Fig. 5b but with tilting frontogenesis associated with the subsidence in Fig. 5e.

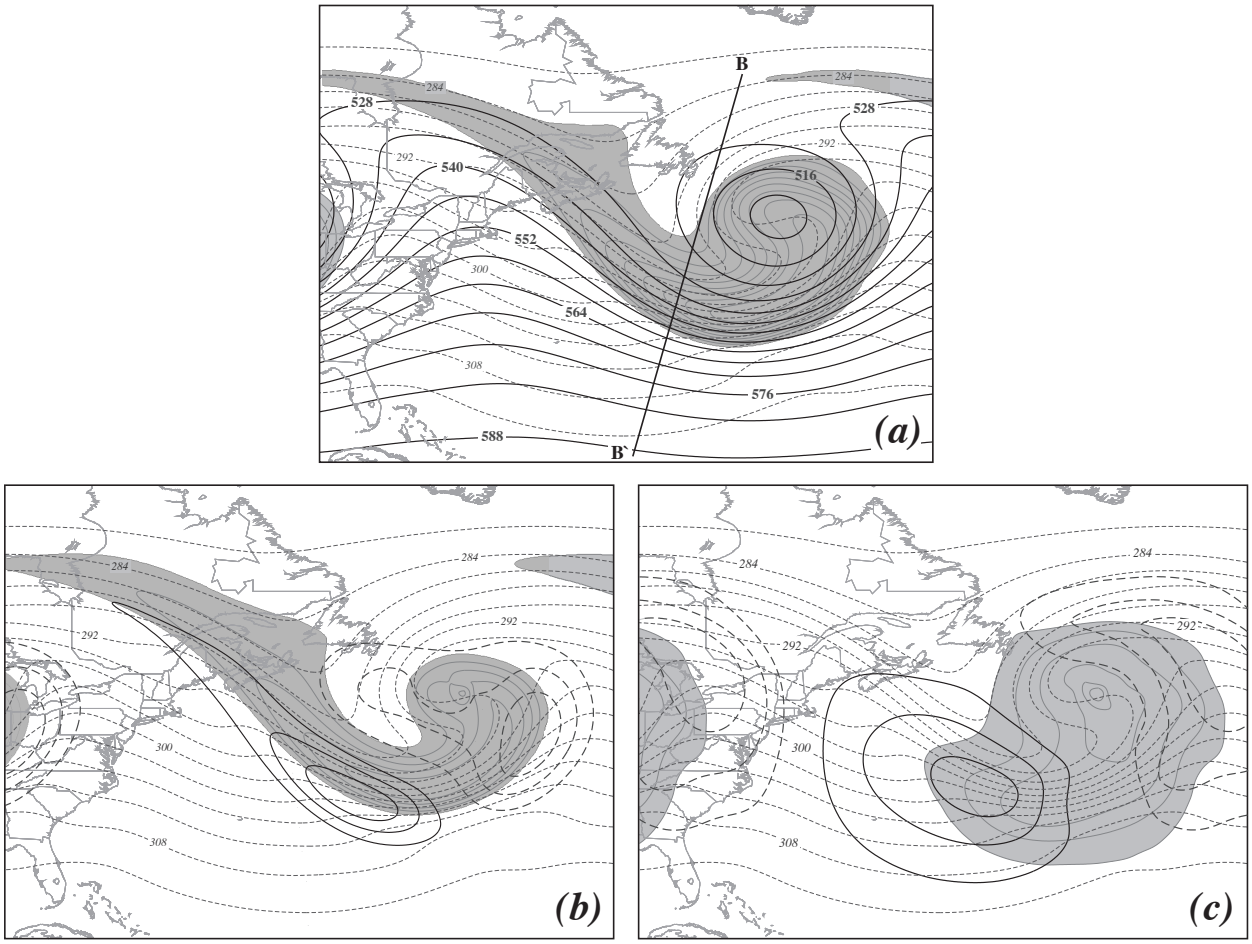

Fig. 6 (a) As for Fig. 4a but from a 42h forecast of the UW-NMS idealized simulation. Vertical cross sections along line B-B` shown in Fig. 7. (b) As for Fig. 4b but from a 42h forecast of the UW-NMS idealized simulation. (c) As for Fig. 4c but from a 42h forecast of the UW-NMS idealized simulation.

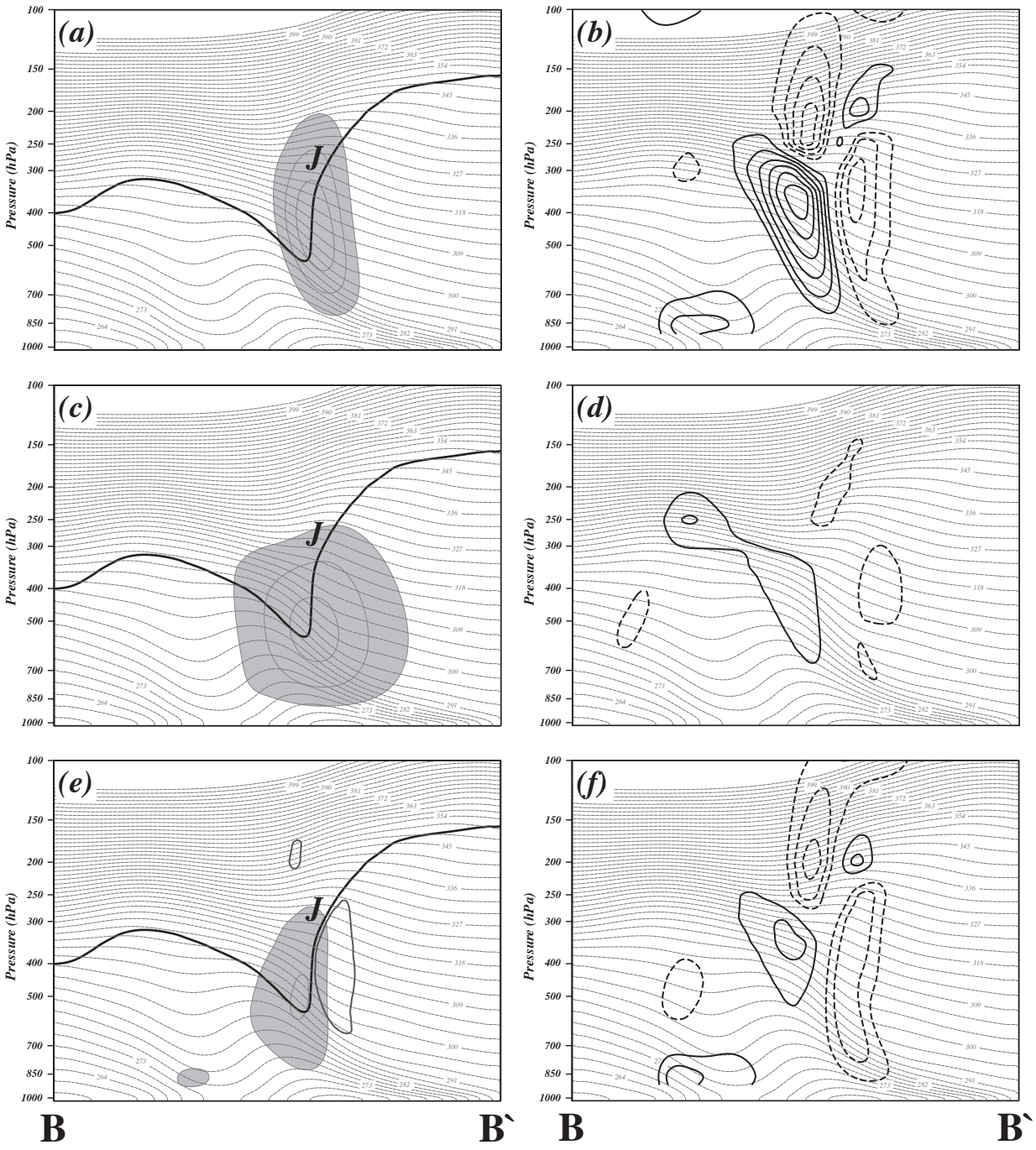

Fig. 7 (a) As for Fig. 5a but along B-B` in Fig. 6a with data from the 42h forecast of the UW-NMS idealized simulation. (b) As for Fig. 5b but along B-B` in Fig. 6a with data from the 42h forecast of the UW-NMS idealized simulation. (c) As for Fig. 5c but along B-B` in Fig. 6a with data from the 42h forecast of the UW-NMS idealized simulation. (d) As for Fig. 5d but along B-B` in Fig. 6a with data from the 42h forecast of the UW-NMS idealized simulation. (e) As for Fig. 5e but along B-B` in Fig. 6a with data from the 42h forecast of the UW-NMS idealized simulation. (f) As for Fig. 5f but along B-B` in Fig. 6a with data from the 42h forecast of the UW-NMS idealized simulation.

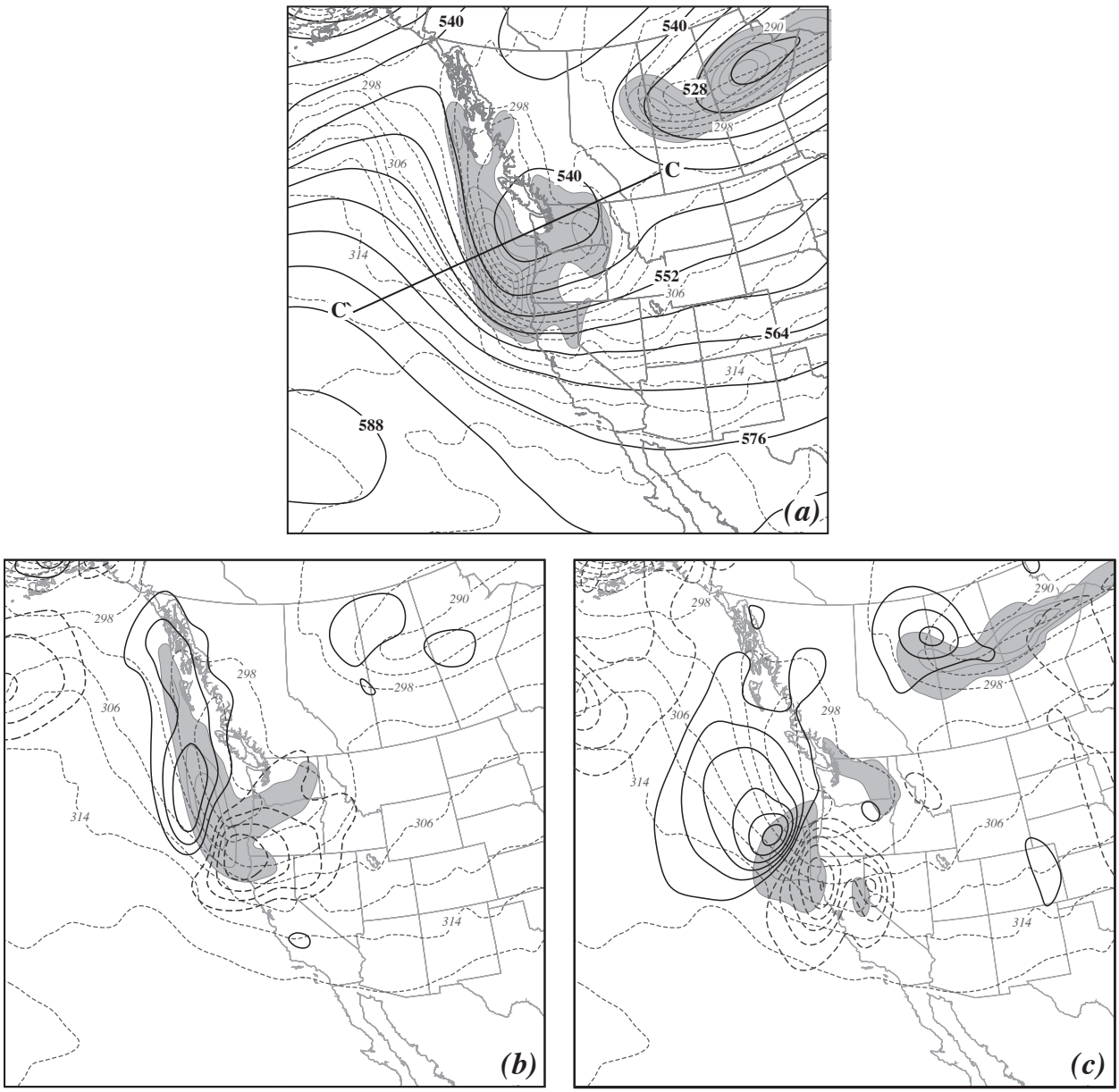

Fig. 8 (a) 500 hPa geopotential height (bold solid lines), potential temperature (dashed lines) and geostrophic vorticity (shaded) from NCEP's Global Forecast System (GFS) analysis valid at 0000 UTC 8 April 2013. Vorticity labeled and contoured in units of 4 x 10^{-5} s^{-1}, beginning at 4 x 10^{-5} s^{-1}. Geopotential height labeled in m and contoured every 60 m. Potential temperature labeled in K and contoured every 2K. Vertical cross sections along line C-C` shown in Fig. 9. (b) 500 hPa geostrophic shear vorticity, potential temperature, and QG ω associated with geostrophic shear vorticity advection by the thermal wind from the GFS analysis valid at 0000 UTC 8 April 2013. Vorticity shaded and contoured as in Fig. 8a. Potential temperature labeled as in Fig. 8a. but contoured every 4K. Solid (dashed) lines are 500 hPa QG ω contoured every 1 (-1) dPa s^{-1} starting at 1 (-1) dPa s^{-1}. (c) As for Fig. 8b but for geostrophic curvature vorticity and QG ω associated with geostrophic curvature vorticity advection by the thermal wind.

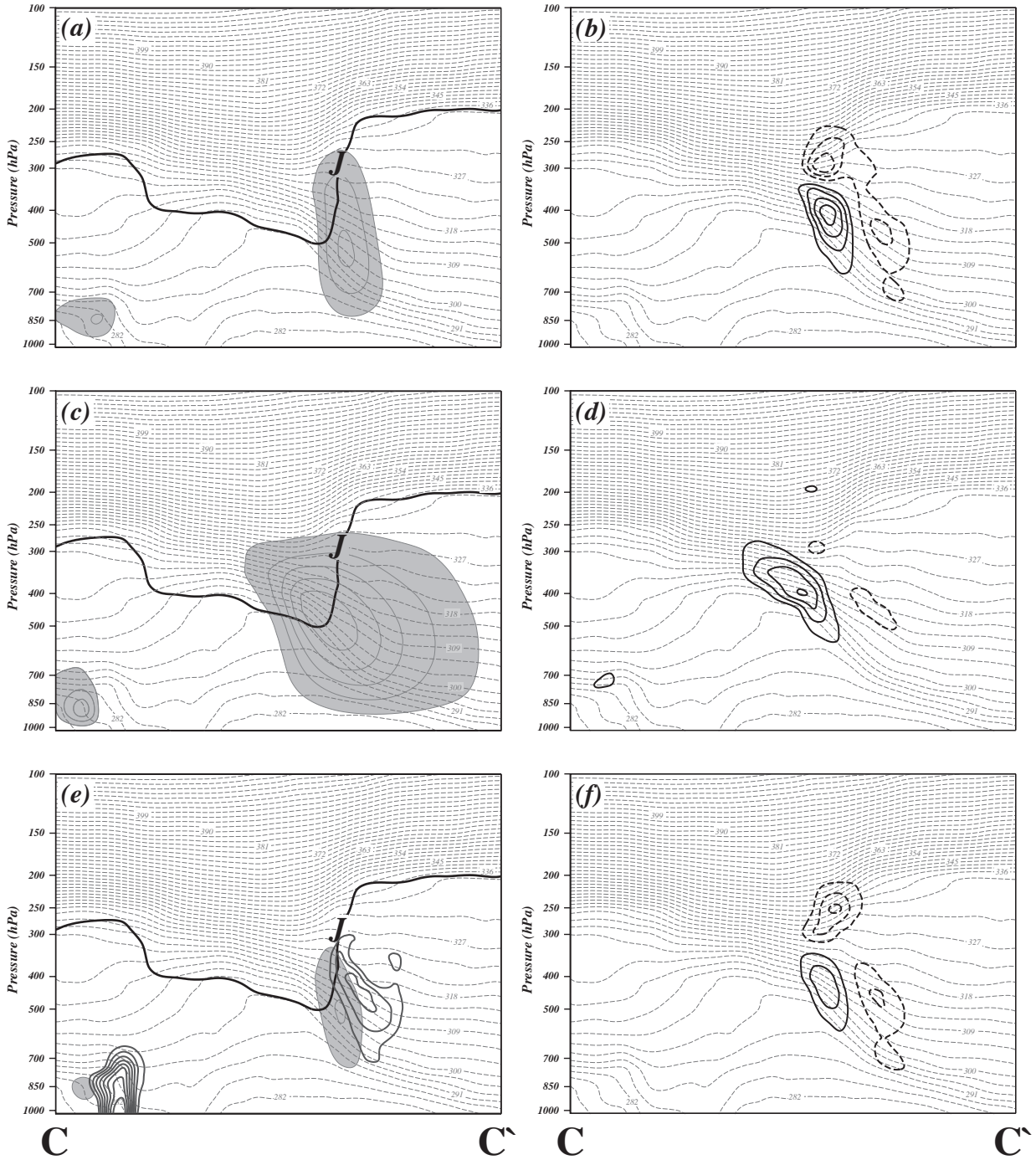

Fig. 9 (a) As for Fig. 5a but along C-C` in Fig. 8a with data from GFS analysis valid at 0000 UTC 8 April 2013. (b) As for Fig. 5b but along C-C` in Fig. 8a with data from the GFS analysis valid at 0000 UTC 8 April 2013. (c) As for Fig. 5c but along C-C` in Fig. 8a with data from the GFS analysis valid at 0000 UTC 8 April 2013. (d) As for Fig. 5d but along C-C` in Fig. 8a with data from the GFS analysis valid at 0000 UTC 8 April 2013. (e) As for Fig. 5e but along C-C` in Fig. 8a with data from the GFS analysis valid at 0000 UTC 8 April 2013. (f) As for Fig. 5f but along C-C` in Fig. 8a with data from the GFS analysis valid at 0000 UTC 8 April 2013.

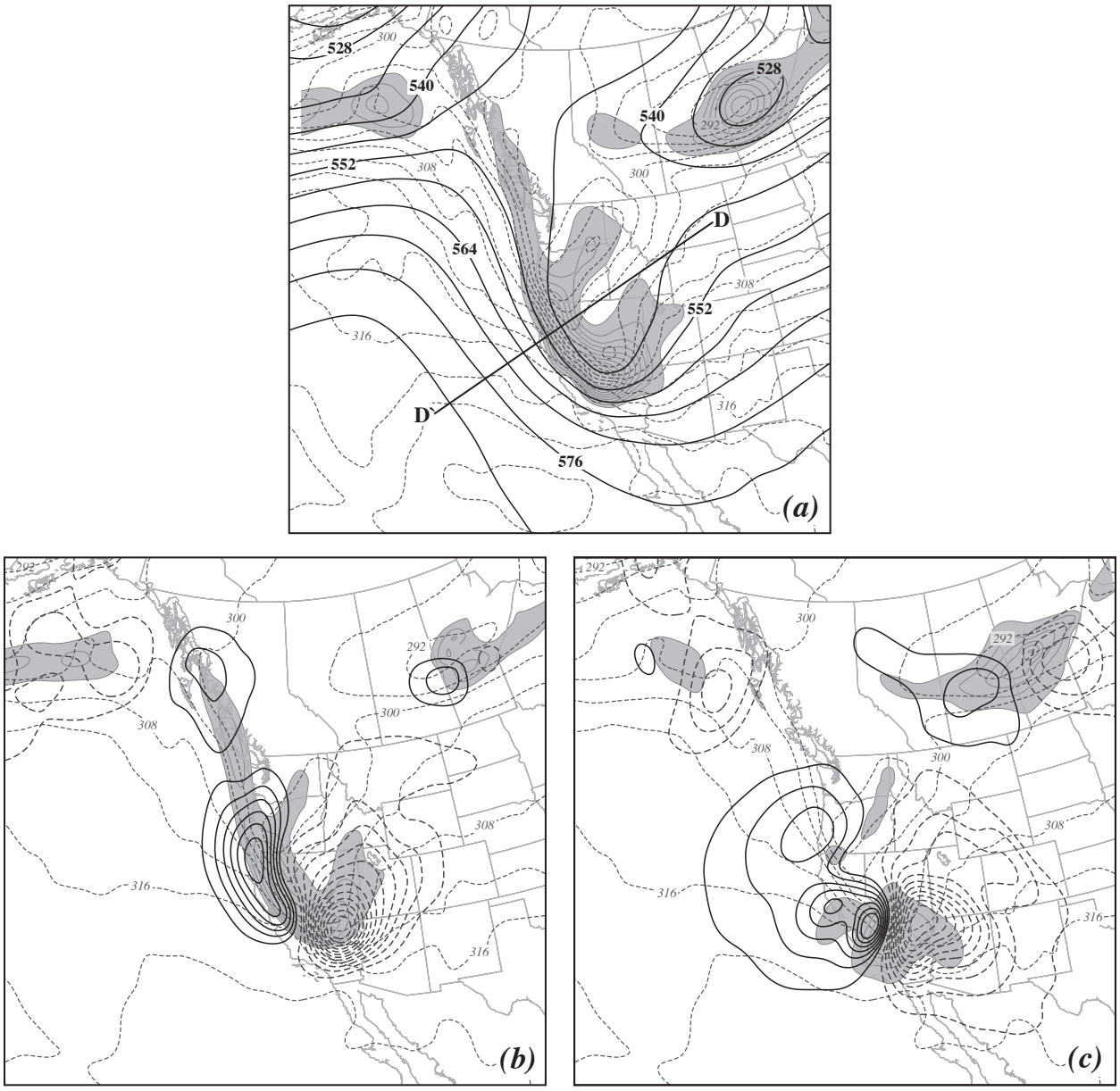

Fig. 10 (a) As for Fig. 8a but from the GFS analysis valid at 1200 UTC 8 April 2013. Vertical cross sections along line D-D` shown in Fig. 11. (b) As for Fig. 8b but from the GFS analysis valid at 1200 UTC 8 April 2013. (c) As for Fig. 8c but from the GFS analysis valid at 1200 UTC 8 April 2013.

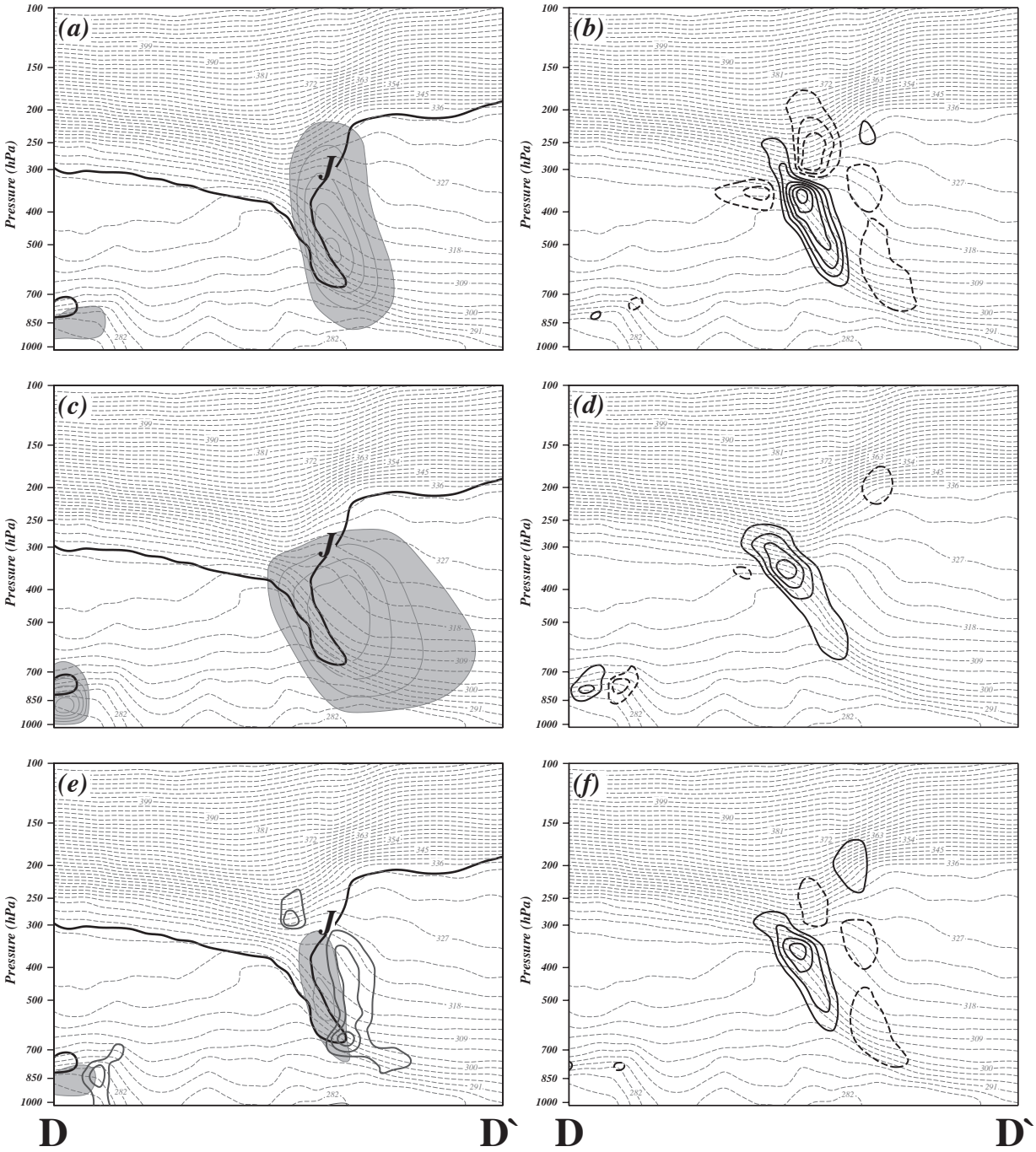

Fig. 11 (a) As for Fig. 5a but along D-D` in Fig. 10a with data from GFS analysis valid at 1200 UTC 8 April 2013. (b) As for Fig. 5b but along D-D` in Fig. 10a with data from the GFS analysis valid at 1200 UTC 8 April 2013. (c) As for Fig. 5c but along D-D` in Fig. 10a with data from the GFS analysis valid at 1200 UTC 8 April 2013. (d) As for Fig. 5d but along D-D` in Fig. 10a with data from the GFS analysis valid at 1200 UTC 8 April 2013. (e) As for Fig. 5e but along D-D` in Fig. 10a with data from the GFS analysis valid at 1200 UTC 8 April 2013. (f) As for Fig. 5f but along D-D` in Fig. 10a with data from the GFS analysis valid at 1200 UTC 8 April 2013.